Asymptotic and numerical analysis of electrohydrodynamic flows of dielectric liquid

Y. K. Suh,[*] K. H. Baek, and D. S. Cho

Department of Mechanical Engineering, Dong-A University, 840 Hadan-dong, Saha-gu, Busan 604-714, Korea

We perform an asymptotic analysis of electrohydrodynamic (EHD) flow of nonpolar liquid subjected to an external, nonuniform electric field. The domain of interest covers the bulk as well as the thin dissociation layers (DSLs) near the electrodes. Outer (i.e., bulk) equations for the ion transport in hierarchical order of perturbation parameters can be expressed in linear form, whereas the inner (i.e., DSL) equations take a nonlinear form. We derive a simple formula in terms of various parameters which can be used to estimate the relative importance of the DSL-driven flow compared with the bulk-driven flow. EHD flow over a pair of cylindrical electrodes is then solved asymptotically and numerically. It is found that in large geometric scale and high ion concentration the EHD flow is dominated by the bulk-charge-induced flow. As the scale and concentration are decreased, the DSL-driven slip velocity increases and the resultant flow tends to dominate the domain and finally leads to flow reversal. We also conduct a flow-visualization experiment to verify the analysis and attain good agreement between the two results with parameter tuning. We finally show, based on the comparison of experimental and numerical solutions, that the rate of free-ion generation (dissociation) should be less than the one predicted from the existing formula.

I. INTRODUCTION

Dielectric liquid is characterized by low conductivity and low electric permittivity due to the nonpolar structure of the constituent molecules. It is used as insulating material in the electric power industry [1–3], as a medium for particle suspension in electrophoretic display [4,5], and as a substance to be electrically pumped [6–10]. In many practical situations, additives such as surfactants are put into the liquid to stabilize the particle suspension or to enhance the material transport [5,11,12].

Figure 1 illustrates the key elements of the physicochemical and electromechanical phenomena of the electrohydrodynamic (EHD) flow of dielectric liquid in the vicinity of the cathode in contact with the liquid. When a surfactant is added to the liquid, free ions are created in the form of reverse micelles [11–14]. The concentrations of free ions (and so the conductivity) increase with the field intensity due to the Onsager effect [12–20]. On the other hand, the free cations and anions are recombined to become ion pairs in the rate proportional to the mobility and inverse of the permittivity. In the bulk, the rate of ion dissociation is basically in equilibrium with that of ion recombination so that the bulk is almost neutralized. However, local variation of the field intensity leads to a nonzero gradient of the ion concentrations, which then causes a relatively small amount of concentration difference between the cation and anion ["bulk charge" in Fig. 1(b)], corresponding to nonuniform field-induced space charge density. The product of the charge density and the electric field serves in the fluid-flow equations as the momentum source, which is responsible for the EHD flow in the bulk ["bulk-driven flow" in Fig. 1(a)]. Such EHD flow phenomena of dielectric fluid associated with the Onsager effect bring physical features that are not found in polar fluid. Saville [21] reviewed the foundation and modeling of EHD flows, and studies on deformation of drops, and hydrodynamic

stability of drops and liquid cylinders, etc.; more recently Suh [14] also reviewed the relevant literature and predicted the importance of the role of thin layers near the electrode at small scales. However, no rigorous study has been given to exploration of the asymptotic analysis on EHD flows of dielectric liquid including both the bulk and the DSL.

Most studies on the EHD flows in dielectric fluid have focused on the bulk-driven flows neglecting the effect of the thin dissociation layers (DSLs) near the electrodes [Fig. 1(a)]. During development of the so-called conduction pumps [6–8], Jeong and Seyed-Yagoobi [22] performed two-dimensional (2D) numerical simulation of EHD flow in an enclosure having a pole-type electrode on the top and a flat electrode on the bottom wall. They included in the simulation the effect of ion dissociation as well as ion recombination, the former being modeled by the Onsager effect. However, their numerical results have not been compared with any experimental data. Successful reproduction of the experimental results of the EHD flow with a theory appeared only recently. Ryu *et al.* [20] first demonstrated that the Onsager effect is responsible for the EHD flow observed over conducting or nonconducting solids subjected to a uniform electric field, and achieved good comparison between the flow visualization and numerical results. Kim *et al.* [10] extended the theory to the pumping of dielectric liquid with a triangular arrangement of three cylindrical electrodes inside a channel. Their experimental results agree well with the numerical calculations not only qualitatively but also quantitatively. However, the validity of the bulk equations used in simulations [10,20] is questionable, in particular for small scales and low ion concentrations, because resultantly they neglected the effect of the charge in thin DSLs near the solids [20] and electrodes [10].

Transport of ions in the DSLs for the nonpolar fluid is similar to that for the polar fluid; counterions are attracted to and coions are repelled from the electrodes [Fig. 1(a)]. Thus, nonequilibrium between ion dissociation and recombination is supposed to yield a charge density which is much higher than that in the bulk ["DSL charge" in Fig. 1(b)]. Localized
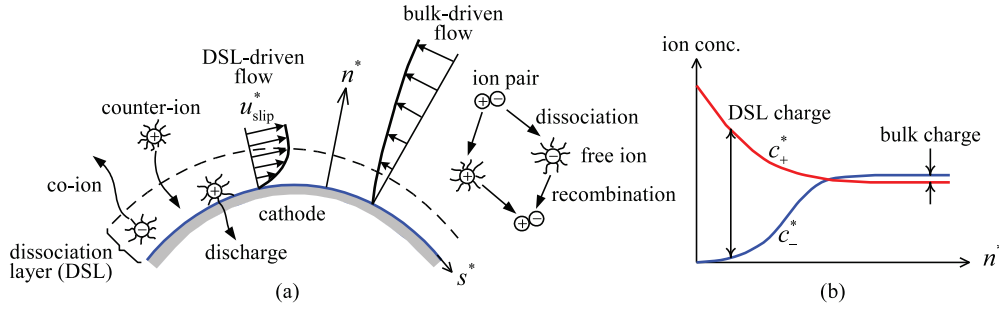
---

[*]yksuh@dau.ac.kr

FIG. 1. (Color online) Schematic illustration of (a) transport and dissociation or recombination of ions, the dramatic difference in the velocity profiles between the bulk-driven and DSL-driven EHD flows, and (b) typical ion-concentration distributions near the cathode.

DSL charge then induces DSL-driven flow, the significance of which depends on several parameters, such as the scale of the problem and the ion concentration. Suh and Baek [23] performed an experimental and numerical study on the EHD flow of a dodecane-Span80 mixture over a pair of coplanar electrodes separated by a gap. They demonstrated that the bulk-charge-driven flow is dominant at a large gap spacing, whereas the DSL-driven flow is dominant at a small gap spacing. They also found that a significant reduction of the recombination constant from the Langevin formula is required for the numerical simulation to successfully yield results matching with the experiment.

Although those recent works [10,20,23] focusing on the fundamental mechanism of EHD flows and parameter adjustment are encouraging in that the experimental results could be successfully reproduced by numerical simulations, a rigorous systematic study on the solution structure has not been reported yet. In this study, therefore, we explore the asymptotic structure of the governing equations consisting of ion-transport equations for the ion concentrations, the Poisson equation for the potential, and Stokes equations for the velocity. We aim to derive simplified governing equations for each order of perturbation parameters separately for the bulk and for the DSL and to understand the way those two solutions match each other. Exploring parameters affecting the competition between the bulk-driven and DSL-driven flows is also one of the main issues to be addressed in this study. As an application, we choose a pair of circular cylinders as electrodes and derive closed-form solutions of the asymptotic equations for the bulk; flat-plate electrodes [23] may provide a benefit in constructing meshes but they suffer from the unavoidable singularity at the plate edges. We also perform 2D numerical simulation with the full equations for the ion-transport and fluid-flow problem in order to verify the asymptotic analysis. Further, we execute experimental visualization and measure the velocity data not only for quantitative verification of the numerical methods but also for parameter tuning.

II. FORMULATION

We consider a pair of electrodes with a characteristic length R submerged in a liquid dielectric with density ρ, viscosity η, and electrical permittivity ε_p. A small amount of surfactant is added to increase the electric conductivity and to enhance the EHD flow [5,11,12]. As usual, it is assumed that free ions are created through the dissociation effect. Without an external

field, the free ions are completely neutralized everywhere and concentrations of cation and anion, c_+^*, c_-^*, are homogeneously distributed in the domain with the zero-field concentration c_0; therefore the fluid velocity $\mathbf{u}^*$ vanishes because of zero induced charge. When a dc voltage difference V_a is applied across the electrodes, concentrations are increased with the local electric-field intensity due to the Onsager effect. Such space-dependent concentration then leads to the creation of charge and EHD flow. The equations governing the development of concentrations of monovalent ions $c_\pm^*$, the electric field $\mathbf{E}^*$, and the fluid velocity $\mathbf{u}^*$ can be written as follows [14,23].

$$\frac{\partial c_+^*}{\partial t^*} + \nabla_* \cdot [(\mathbf{u}^* + \mu_+ \mathbf{E}^*)c_+^*] - D_+ \nabla_*^2 c_+^*$$
$$= w^* - \alpha c_+^* c_-^*, \tag{1a}$$

$$\frac{\partial c_-^*}{\partial t^*} + \nabla_* \cdot [(\mathbf{u}^* - \mu_- \mathbf{E}^*)c_-^*] - D_- \nabla_*^2 c_-^*$$
$$= w^* - \alpha c_+^* c_-^*, \tag{1b}$$

$$\varepsilon_p \nabla_* \cdot \mathbf{E}^* = e(c_+^* - c_-^*) \equiv q^*, \tag{1c}$$

$$\rho \left[\frac{\partial \mathbf{u}^*}{\partial t^*} + (\mathbf{u}^* \cdot \nabla_*) \mathbf{u}^* \right]$$
$$= -\nabla_* p^* + \eta \nabla_*^2 \mathbf{u}^* + q^* \mathbf{E}^*, \tag{1d}$$

$$\nabla_* \cdot \mathbf{u}^* = 0, \tag{1e}$$

where $\mu_\pm$ is the ion mobility, $D_\pm$ the diffusivity, $w^* = w_0 F(E^*; \gamma^*)$ the local ion-dissociation rate, $w_0 = \alpha c_0^2$ the zero-field dissociation rate, $q^* = e(c_+^* - c_-^*)$ the space charge density, α the ion-recombination constant, and e the elementary charge. The mobility $\mu_\pm$ is related to the ionic radius $a_\pm$ by $\mu_\pm = e/(6\pi \eta a_\pm)$ and to the diffusivity by $\mu_\pm = D_\pm/\varsigma_T$, where $\varsigma_T = k_B T/e$ is the thermal potential, k_B the Boltzmann constant, and T the temperature; so, once $a_\pm$ is set, it automatically determines $\mu_\pm$ and $D_\pm$.

The function $F(E^*; \gamma^*)$ to be called "Onsager function" reads [14]

$$F(E^*; \gamma^*) = \sum_{k=0}^{\infty} \frac{(4\gamma^* E^*)^k}{k!(k+1)!}. \tag{2}$$

We note that F monotonically increases with the field intensity. The Onsager constant γ^* is to be determined with a reduction factor κ_O from $\gamma^* = \kappa_O \gamma_O^*$, where $\gamma_O^* \equiv e/(16\pi \varepsilon_p \varsigma_T^2)$ corresponds to the original Onsager constant; we open here the possibility of tuning γ^* based on the literature showing discrepancy between the Onsager theory and the experimental

data. Onsager theory has long been accepted as an appropriate model for the conductivity enhancement at high electric field. It, on the other hand, overestimates the conductivity in particular at high field as shown in [24] for an acid solution. They attributed the discrepancy to the hydrodynamic interaction between ions neglected in the Onsager theory. The overestimation of the theory is also reported for nonpolar liquid, such as dodecane in [25]. Onsager theory is also reported to significantly underestimate the conductivity of a highly purified water in [26]. Zhakin [27] addresses the discrepancy in the field-enhanced conductivity between the experimental data and the Onsager theory and the possible improvement of the theory by considering the finite size of ions, instead of point ions. Variation of the Onsager parameter (in fact γE in the present terminology) is also tried to fit the experimental data of the conductivity of the silicone oil [28].

The recombination constant α is determined from $\alpha = \kappa_L \alpha_L$, where κ_L is a control parameter, $\alpha_L = 2e\bar{\mu}/\varepsilon_p$ the Langevin constant, and $\bar{\mu} = (\mu_+ + \mu_-)/2$ the averaged mobility. In our previous study on the EHD flow over coplanar electrodes [23], we have shown that for successful qualitative and quantitative matching between experimental and numerical results, α should be substantially reduced from α_L. We will also experience in this study a similar necessity of parameter tuning.

Under the assumption of steady state, Eqs. (1a)–(1e) can be written in terms of dimensionless variables as follows.

$$\varepsilon\{\nabla\cdot[(\mathbf{u}+m_+\mathbf{E})c_+] - m_+\delta\nabla^2 c_+\} = 2\kappa_L[F(E;\gamma) - c_+c_-],$$
(3a)

$$\varepsilon\{\nabla\cdot[(\mathbf{u}-m_-\mathbf{E})c_-] - m_-\delta\nabla^2 c_-\} = 2\kappa_L[F(E;\gamma) - c_+c_-],$$
(3b)

$$\varepsilon\nabla\cdot\mathbf{E} = c_+ - c_- \equiv q,$$
(3c)

$$\mathrm{Re}(\mathbf{u}\cdot\nabla)\cdot\mathbf{u} = -\nabla p + \nabla^2\mathbf{u} + Mq\mathbf{E},$$
(3d)

$$\nabla\cdot\mathbf{u} = 0.$$
(3e)

Here, the spatial coordinates are scaled by R, the concentrations by c_0, the field by V_a/R, the space charge density by ec_0, the velocity by $\bar{\mu} V_a/R$, and the pressure by $\eta\bar{\mu} V_a/R^2$. Dimensionless parameters involved in Eqs. (3a)–(3e) are Reynolds number $\mathrm{Re} = \rho\bar{\mu} V_a/\eta$, the body-force factor $M = ec_0R^2/(\eta\bar{\mu})$, the DSL thickness $\varepsilon = \varepsilon_p V_a/(ec_0R^2)$, the mobility $m_\pm = \mu_\pm/\bar{\mu}$, the diffusion parameter $\delta = \varsigma_T/V_a$, and half of the distance between the electrodes $d = d^*/R$. Further, $\gamma = \gamma^* V_a/R$ is the dimensionless Onsager constant.

We need boundary conditions to solve Eqs. (3a)–(3e). The simplest but most plausible conditions for the concentrations may be that cations and anions are completely depleted on the cathode and anode, respectively [6–8,23]:

$$c_+ = 0 \ \text{on} \ \partial\Omega_+, \quad c_- = 0 \ \text{on} \ \partial\Omega_-,$$

where $\partial\Omega_\pm$ denotes the electrode surface. If we assume $\delta \ll 1$ (typically $\delta = 5 \times 10^{-5}$) and neglect the diffusion terms, as is done in our asymptotic solution in the following section, we do not need boundary conditions for counterion concentration on each electrode. In the numerical simulation of the full two-dimensional (2D) equations with a nonzero value for δ, however, we may apply either $\partial c_+/\partial n = 0$ or

$\partial^2 c_+/\partial n^2 = 0$ upon convenience, e.g., on the cathode, but no significant difference should occur if δ remains negligibly small. The fundamental reason for neglecting the diffusion terms can be explained in terms of the normal component of the dimensionless flux of counterions at the cathode wall, $J_{+n} = -m_+(E_n c_+ - \delta\,\partial c_+/\partial n)$, where the subscript n denotes the normal component, and the fluid's impermeable condition has been applied. If the zero-flux condition, $J_{+n} = 0$, were to be applied, we expect that $\partial c_+/\partial n$ must be very large in $O(\delta^{-1})$ within the thin layer of $O(\delta)$, for the balancing between the two terms. However, the zero-flux condition must be abandoned because complete screening of the electrode by the accumulation of counterions would then result in the zero field and zero current, which is not the case (see, e.g., [11,12]). In fact, in this study we allow free charge of counterions such that $\delta|\partial c_+/\partial n| \ll |E_n|c_+$. This can be achieved by specifying either $\partial c_+/\partial n = 0$ or $\partial^2 c_+/\partial n^2 = 0$ on the cathode.

III. ASYMPTOTIC SOLUTION METHOD

For asymptotic analysis to be feasible, we assume that the convective and diffusive terms in Eqs. (3a) and (3b) are negligible and $\varepsilon \ll 1$ (typically $\varepsilon = 7 \times 10^{-4}$). Since a small parameter ε multiplies to the highest derivatives in each of Eqs. (3a)–(3c), we expect thin layers, i.e., DSLs, near the electrodes. In this section, we present the structure of the solutions in the bulk and DSL by using the asymptotic analysis. Since the velocity is scaled by the typical ion-migration speed, $\bar{\mu} V_a/R$, we expect $|\mathbf{u}| \ll 1$; as will be shown later, $|\mathbf{u}| = O(\varepsilon)$. The effective Reynolds number is then of $O(\varepsilon)$ because Re is of $O(1)$. Thus we can neglect the convective terms in the ion-transport equations so that they are decoupled from the fluid-flow problem. Further, neglecting the diffusive terms, we can write Eqs. (3a)–(3c) as follows.

$$c_+c_- = F - \varepsilon\tilde{m}_+\nabla\cdot(c_+\mathbf{E}), \quad (4a)$$

$$c_+ - c_- = \varepsilon\nabla\cdot\mathbf{E}, \quad (4b)$$

$$\nabla\cdot[(\tilde{m}_+c_+ + \tilde{m}_-c_-)\mathbf{E}] = 0, \quad (4c)$$

where $\tilde{m}_\pm = m_\pm/(2\kappa_L)$ is the modified mobility.

A. Bulk solution

In order to get the asymptotic solutions of Eqs. (4a)–(4c) for small ε, we expand the variables as

$$(c_+, c_-, \mathbf{E}) = \sum_{i=0}^{\infty} \varepsilon^i(f_i, g_i, \mathbf{E}_i),$$

where $(f_i, g_i, \mathbf{E}_i)$ are again expanded for small γ as

$$(f_i, g_i, \mathbf{E}_i) = \sum_{j=0}^{\infty} \gamma^j(f_{ij}, g_{ij}, \mathbf{E}_{ij}).$$

$F(E;\gamma)$ is then expanded as

$$F(E) = F_0 + \varepsilon F_1 + \varepsilon^2 F_2 + \cdots,$$

where

$$F_0 = 1 + 2\gamma H_{00} + \gamma^2(2H_{01} + 4H_{00}^2/3) + \cdots,$$
$$F_1 = 2\gamma H_{10} + \gamma^2(2H_{11} + 8H_{00}H_{10}/3) + \cdots,$$

$$F_2 = 2\gamma H_{20} + \gamma^2\left(2H_{21} + 8H_{00}H_{20}/3 + 4H_{10}^2/3\right) + \cdots.$$

A detailed formula for the expression of H_{ij} is given in Appendix A. We also need the expansion for $\sqrt{F_0}$:

$$\sqrt{F_0} = 1 + \gamma H_{00} + \gamma^2\left(H_{01} + H_{00}^2/6\right) + \cdots.$$

Substituting these into Eqs. (4a)–(4c), we obtain the following equations for f_0, g_0, and $\mathbf{E}_0$:

$$f_0 = g_0 = \sqrt{F_0}, \tag{5a}$$

$$\nabla \cdot (f_0\mathbf{E}_0) = 0. \tag{5b}$$

To solve these nonlinear equations, we may use a numerical method. Depending on the simplicity of the geometry of the given problem, we may attempt an analytic-solution method for (5a) and (5b) by using the double expansions of the variables. Then we get the following for f_0, g_0, and $\mathbf{E}_0$.

$$f_{00} = g_{00} = 1, \tag{6a}$$

$$\nabla \cdot \mathbf{E}_{00} = 0, \tag{6b}$$

$$f_{01} = g_{01} = H_{00}, \tag{7a}$$

$$\nabla \cdot \mathbf{E}_{01} = -\mathbf{E}_{00} \cdot \nabla E_{00}, \tag{7b}$$

$$f_{02} = g_{02} = H_{01} + \tfrac{1}{6}H_{00}^2, \tag{8a}$$

$$\nabla \cdot \mathbf{E}_{02} = -\nabla \cdot (f_{01}\mathbf{E}_{01} + f_{02}\mathbf{E}_{00}), \tag{8b}$$

and so on.

Next, the equations for the three unknowns f_1, g_1, and $\mathbf{E}_1$ are

$$f_0(f_1 + g_1) = F_1, \tag{9a}$$

$$f_1 - g_1 = \nabla \cdot \mathbf{E}_0 \equiv q_1, \tag{9b}$$

$$(\tilde{m}_+ + \tilde{m}_-)\nabla \cdot (f_0\mathbf{E}_1) = -\nabla \cdot [(\tilde{m}_+ f_1 + \tilde{m}_- g_1)\mathbf{E}_0]. \tag{9c}$$

In passing, note that after solving Eqs. (5a) and (5b), we can get the leading-order charge density q_1 from $q_1 = \nabla \cdot \mathbf{E}_0 = -\mathbf{E}_0 \cdot \nabla(\ln f_0)$ as seen from Eqs. (9b) and (5b). Further, following Eq. (5a), the concentration f_0 increases monotonically with the field intensity E. So, we can say, in the $O(\varepsilon)$, that the dimensionless space charge density εq_1 is negative when the field intensity increases in the direction of the field vector, and vice versa.

When expansions for small γ are again used for variables f_1, g_1, and $\mathbf{E}_1$, we get

$$f_{10} = g_{10} = 0, \tag{10a}$$

$$\nabla \cdot \mathbf{E}_{10} = 0, \tag{10b}$$

$$f_{11} + g_{11} = 2\mathbf{E}_{00} \cdot \mathbf{E}_{10}/E_{00}, \tag{11a}$$

$$f_{11} - g_{11} = \nabla \cdot \mathbf{E}_{01} \equiv q_{11}, \tag{11b}$$

$$\nabla \cdot \mathbf{E}_{11} = -\nabla \cdot (E_{00}\mathbf{E}_{10}) - \nabla \cdot [(f_{11} + g_{11})\mathbf{E}_{00}/2], \tag{11c}$$

and so on. The space charge density q is then determined by

$$q = \varepsilon \gamma (q_{11} + \gamma q_{12} + \gamma^2 q_{13} + \cdots) + O(\varepsilon^2), \tag{12}$$

where $q_{1j} = \nabla \cdot \mathbf{E}_{0j}$. We can see from this formula that the leading-order term of the space charge density is $O(\varepsilon\gamma)$.

The analytic-solution procedure can be summarized as follows. First, we obtain the potential ϕ_{00} and subsequently the field $\mathbf{E}_{00}$ from the solution of $\nabla^2\phi_{00} = 0$ with potentials

specified at each of the electrode surfaces. This then gives f_{01} via Eq. (7a). Next, we obtain ϕ_{01} and $\mathbf{E}_{01}$ by solving Eq. (7b), or $\nabla^2\phi_{01} = \mathbf{E}_{00} \cdot \nabla E_{00}$ with homogeneous boundary conditions for ϕ_{01}, which in turn gives f_{02} via Eq. (8a). In this way, we repeat the solution procedure up to the required order of γ. Then, we get q_{1j} and q from Eq. (12). In all cases treated in this study, the leading-order solutions of $O(\varepsilon^0)$ are accurate enough.

Once the space charge density is determined, the body-force terms $Mq\mathbf{E}$ in the Navier-Stokes equations can be evaluated and then used in calculating the velocity field. Analytically solving the Navier-Stokes equations (3d) is possible only in rare cases, and in general we must resort to the numerical method. Nevertheless, the order of magnitude of the bulk velocity, u_b, can be readily estimated from Eq. (3d) as $u_b \sim \varepsilon\gamma M$ or in dimensional quantity,

$$u_b^* \sim \frac{\varepsilon_p\gamma_O^*}{\eta}\kappa_O R\left(\frac{V_a}{R}\right)^3. \tag{13}$$

So, we see that the bulk velocity increases in cubic power of the reference field, which is supposed to be in the same order of magnitude as the applied field. This has been experimentally shown by [10,20]. It also increases with the Onsager factor κ_O and the reference length R.

Based on the above asymptotic analysis, we can present more robust simplified bulk equations for the electric field, modified from the solution of $\nabla \cdot \mathbf{E}^* = 0$ due to the Onsager effect, as follows.

$$\nabla \cdot [\mathbf{E}^*\sqrt{F(E^*;\gamma^*)}] = 0, \tag{14}$$

which is valid in $O(\varepsilon)$. Note that no Onsager effect means $F = 1$. After solving this nonlinear equation for $\mathbf{E}^*$ (or practically for the potential ϕ^*), the charge density is obtained from

$$q^* = \frac{-\mathbf{E}^* \cdot \nabla\sqrt{F}}{\sqrt{F}}. \tag{15}$$

In [10,20], Eq. (14) is employed with a simple approximation, $\sqrt{F} \cong 1 + \gamma H_{00}$, to get the space charge density and subsequently the fluid flow. Such a simplified formula, however, is applicable to the relatively low field problems as will be seen in Sec. IV B. We will also see that the bulk solutions alone, without considering the DSL effect, cannot match the experimental results for small scales and low concentrations.

B. Dissociation-layer solution

Contrary to the bulk, the DSL can produce nonzero space charge density in the $O(\varepsilon^0)$ equations. We assume that DSL is very thin compared with the reference length and the tangential gradient $\partial\hat{\varphi}/\partial s$ for any dimensionless DSL variable $\hat{\varphi}$ is much smaller than the normal gradient $\partial\hat{\varphi}/\partial n$, where n and s are dimensionless normal and tangential coordinates, respectively, on the electrode surface; we attach hats to the dependent variables for the DSL equations. Further, we introduce a stretched variable Y for the normal coordinate n such that $n =$

$\varepsilon[E_{0b}/(2\kappa_L\sqrt{F_{0b}})]Y$. As in the bulk solution, we expand the DSL variables as $(\hat{c}_+,\ \hat{c}_-,\ \hat{E}_n) = (\sqrt{F_{0b}}\hat{f},\ \sqrt{F_{0b}}\hat{g},\ E_{0b}\hat{h}) + O(\varepsilon)$. Then the leading-order equations read

$$m_+\frac{d(\hat{h}\hat{f})}{dY} + \hat{f}\hat{g} = \frac{F_0}{F_{0b}}, \tag{16a}$$

$$-m_-\frac{d(\hat{h}\hat{g})}{dY} + \hat{f}\hat{g} = \frac{F_0}{F_{0b}}, \tag{16b}$$

$$2\kappa_L\frac{d\hat{h}}{dY} - \hat{f} + \hat{g} = 0. \tag{16c}$$

The functions $F_{0b}(s)$ and $E_{0b}(s)$ are given from evaluation of the bulk solutions $F_0(x,y)$ and $E_0(x,y)$ on the electrode wall. Boundary conditions are $\hat{g} = 0$ at $Y = 0$ and $\hat{h} \to -1$ as $Y \to \infty$ for the cathode wall ($\hat{f} = 0$ at $Y = 0$ and $\hat{h} \to 1$ as $Y \to \infty$ for the anode wall), and $(\hat{f}, \hat{g}) \to (1, 1)$ as $Y \to \infty$ regardless of the electrode polarity. Note that the term F_0/F_{0b} in Eqs. (16a) and (16b) is a function of both s and Y and so are $(\hat{f}, \hat{g}, \hat{h})$. Under the limit $\gamma \to 0$, however, F_0/F_{0b} tends to 1 and thus the DSL variables are only functions of Y. In this study, the nonlinear one-dimensional (1D) ordinary differential Eqs. (16a)–(16c) (to be called "DSL equations" hereafter) are solved using a numerical method [14]. Arbitrary transient terms are added to the left-hand side (LHS) of Eqs. (16a) and (16b) in order to overcome numerical instability through the relaxation effect. A second-order upwind method is used to discretize the conduction (first) terms of Eqs. (16a) and (16b), while the central difference scheme is employed for the first term of Eq. (16c), which is rewritten in terms of the localized potential $\hat{\phi}$ as $-2\kappa_L d^2\hat{\phi}/dY^2$; $\hat{\phi}$ is related to the dimensional potential ϕ^* (defined as $\mathbf{E}^* = -\nabla_*\phi^*$) by $\phi^* = [\varepsilon E_{0b}^2 V_a/(2\kappa_L\sqrt{F_{0b}})]\hat{\phi}$. Boundary conditions as well as the discretization schemes of the conduction terms take different forms for different electrode polarities. In the following, we explain the numerical methods for the DSL equations near the cathode. In solving Eq. (16b) for $\hat{g}$, the variables $\hat{f}$ and $\hat{h}$ are treated known, and calculation is performed marching from the cathode wall $Y = 0$, where the boundary condition is specified as $\hat{g} = 0$, toward the end of the computational domain, $Y = Y_m$; in this study we take $Y_m = 10$. On the contrary, in solving Eq. (16a) for $\hat{f}$, the variables $\hat{g}$ and $\hat{h}$ are treated as known, and we march from $Y = Y_m$ where the boundary condition is specified as $\hat{f} = 1$ toward the cathode wall. Boundary conditions of $\hat{\phi}$ at $Y = 0$ can be taken as arbitrary, and we set $\hat{\phi} = 0$ there. At $Y = Y_m$, we set $d\hat{\phi}/dY = 1$. When the DSL solutions near the anode are to be obtained, we can either run a code specifically designed for the anode or run the code for the cathode but with m_+ and m_- assigned with the actual values of m_- and m_+, respectively, and understand the given results $(\hat{f}, \hat{g}, \hat{h})$ as $(\hat{g}, \hat{f}, -\hat{h})$.

In order to understand the nature of the DSL solutions, we present, in Fig. 2, the numerical results of 1D simulation of the DSL equations (16a)–(16c) near the cathode given with $m_{\pm} = 1$ and under the limit $\gamma \to 0$; then, the given solutions are universal in that they are independent of any parameter. Here, f_w and h_w denote the values of $\hat{f}$ and $\hat{h}$, respectively, evaluated on the cathode wall. Y_e stands for the dimensionless thickness of the DSL where $\hat{g} = 0.99$. We can see from this
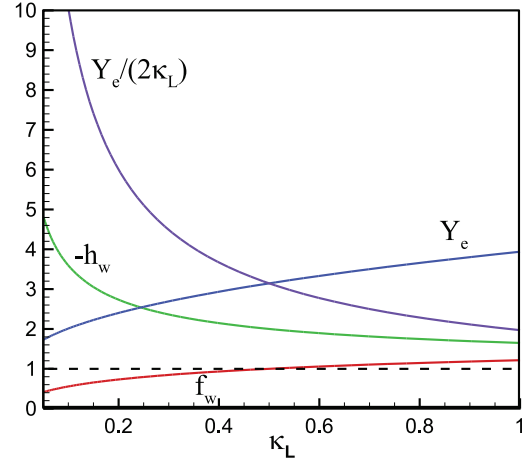

FIG. 2. (Color online) Dimensionless counterion concentration (f_w) and negative electric field ($-h_w$) evaluated on the cathode wall given from the simulation of the 1D ion-transport problem within DSL for $m_{\pm} = 1$ and $\gamma = 0$. Also shown is Y_e, the Y coordinate of the DSL edge, and the dimensionless quantity $Y_e/(2\kappa_L)$ which is proportional to the actual DSL thickness n_e^*.

figure that both f_w and $-h_w$ are larger than 1 at $\kappa_L = 1$. The former decreases as κ_L is decreased, and at roughly $\kappa_L < 0.5$ it becomes less than 1, which will also be proven from simple asymptotic solutions in Sec. IV B. The value $-h_w$, however, increases monotonically as κ_L is decreased. The influence of κ_L on the charge density and the momentum force in the DSL can also be understood from this figure. The dimensionless charge density is proportional to $\hat{f} - \hat{g}$ and so it should be approximately proportional to f_w because $g_w = 0$. However, since both $-h_w$ and the effective dimensionless DSL thickness $Y_e/(2\kappa_L)$ increases very sharply as κ_L is decreased, we expect that the momentum force (product of the charge density and the field) would increase as κ_L is decreased. Now, it can be shown that under the plausible assumption $Y_e = $ constant and the limit $\gamma \to 0$, the dimensionless DSL thickness can be estimated by

$$n_e \sim \frac{\varepsilon_p E_{0b}^*}{e\kappa_L c_0 R} = \left(\frac{\varepsilon}{\kappa_L}\right)\left(\frac{E_{0b}^*}{V_a/R}\right). \tag{17}$$

Thus it increases as each of κ_L, c_0, and R is decreased or the local bulk field intensity E_{0b}^* is increased. On the other hand, note that the magnitude of the charge density within the DSL is of $O(1)$ but it is confined to the thin DSL in $O(\varepsilon)$. On the contrary, Eq. (12) indicates that the magnitude of the bulk-charge density is small in $O(\varepsilon\gamma)$ but it covers the bulk of the size in $O(1)$. Thus, curiosity arises as to how those two effects are competitive in determining the EHD flow around the electrodes. The question may be answered by considering the slip velocity which is a manifestation of the DSL effect.

C. Slip velocity and slip-velocity model

Let us look into the momentum equations to determine the slip velocity at the edge of the DSL. In addition to the condition $|\partial\hat{\varphi}/\partial s| \ll |\partial\hat{\varphi}/\partial n|$, we assume that the normal component of the velocity $\hat{u}_n$ can be neglected when compared with the

tangential component $\hat{u}_s$. Then, Eq. (3d) becomes

$$\frac{\partial \hat{p}}{\partial s} = \frac{\partial^2 \hat{u}_s}{\partial n^2} + M\hat{q}\,\hat{E}_s, \tag{18a}$$

$$\frac{\partial \hat{p}}{\partial n} = M\hat{q}\,\hat{E}_n. \tag{18b}$$

Applying the relation $\hat{q} \cong \varepsilon \frac{\partial E_n}{\partial n}$, we can integrate Eq. (18b) to get $\hat{p} = \varepsilon M E_{0b}^2(\hat{h}^2 - 1)/2$, where $E_{0nb}^2 \cong E_{0b}^2$ is assumed and $\hat{p}$ is taken zero at the DSL edge. Differentiating this with respect to s and substituting the result into Eq. (18a), we obtain

$$\frac{\partial^2 \hat{u}_s}{\partial n^2} = \frac{\varepsilon M}{2} \frac{\partial}{\partial s}\left[E_{0b}^2(\hat{h}^2 - 1)\right]$$
$$+ \frac{\varepsilon M}{2\kappa_L}\sqrt{F_{0b}}(\hat{f} - \hat{g})\frac{\partial}{\partial s}\left[\left(E_{0b}^2/\sqrt{F_{0b}}\right)\hat{\phi}\right], \tag{19}$$

where $\hat{E}_s$ in Eq. (18a) has been written in terms of the potential drop in the DSL near the anode (or potential rise for the cathode) $\hat{\phi}$. Integrating Eq. (19) twice with respect to n under the no-slip condition on the wall ($\hat{u}_s = 0$ at $n = 0$) and the far-field condition ($\partial \hat{u}_s/\partial n \to 0$ as $n \to \infty$) gives us the slip velocity u_{slip}. For practical purposes, however, we must employ a numerical method to integrate (19) twice with respect to n to get the slip velocity.

The first term of Eq. (19) comes from the osmotic-pressure effect, while the second comes from the tangential variation of the potential drop in the DSL of the anode (or potential rise for the cathode). In the derivation of the classical Helmholtz-Smoluchowski (HS) formula (see, e.g., [29]) for the slip velocity of the polar fluid, the contribution of the osmotic-pressure term is after all canceled out by a part of the tangential Coulombic-force term, and more importantly the remaining body-force term in the tangential component of the momentum equations can be readily integrated twice with respect to the normal coordinate, yielding to a very compact form for the slip velocity. This holds not only for the case where a fixed charge is specified at the dielectric wall (classical electro-osmosis, [29]) but also for the case where a constant potential is applied at the electrode (induced-charge electro-osmosis, [30–36]). Mathematically, it can be shown that the very compact formulation for the HS slip velocity of the polar fluid comes from the fact that in the diffuse layer of EDL the ion concentration is related to the potential through the Boltzmann distribution law [29–32], which is again the outcome of the equilibrium between the conduction and diffusion terms in the ion-transport equations. For the EHD flow of nonpolar fluid, however, the DSL shows equilibrium between the conduction and ion-dissociation and recombination terms, and thus the situation is different from that with polar fluids.

Noting n is of $O(\varepsilon/\kappa_L)$ and assuming that both the first and the second terms on the right-hand side (RHS) of Eq. (19) are of $O(\varepsilon M)$ (numerically we will see in Sec. IV B that this is correct), we can derive $u_{\text{slip}} \sim \varepsilon^3 M/\kappa_L^2$, or in dimensional quantity,

$$u_{\text{slip}}^* \sim \frac{\varepsilon_p^3}{\eta e^2} \frac{(V_a/R)^4}{\kappa_L^2 c_0^2 R}. \tag{20}$$

Thus, the slip velocity induced by the DSL charging increases in the fourth power of the reference field. It also increases as

the Langevin factor κ_L, or the zero-field concentration c_0 or the reference length R is decreased. Then, from Eqs. (13) and (20) we get

$$\frac{u_{\text{slip}}^*}{u_b^*} \sim \frac{\varepsilon_p^3 \varsigma_T^2}{e^3} \frac{V_a/R}{\kappa_O \kappa_L^2 c_0^2 R^2}. \tag{21}$$

So, we can say that, under the assumption of a fixed reference field V_a/R, the role of DSL referred to that of the bulk in determining the flow field increases as c_0 and R of the problem decrease. It also increases as $1/(\kappa_O \kappa_L^2)$ as the factors κ_O and κ_L are decreased.

We are now ready to propose a slip-velocity model, where the conventional bulk-solution method [10,20] is improved by imposing slip velocity on the electrode walls in solving the fluid-flow problem; we still take the benefit of being free from solving the ion-transport equations in the bulk. Following the in-depth analysis given so far, we first solve the nonlinear bulk equation (14), which being decoupled from the DSL equations constitutes a purely electrical problem; such 2D simulation with the bulk equation (14) will be referred to as B2D. The one-dimensional DSL equations are next solved with the local electric-field intensity evaluated at $n = 0$ from B2D solutions serving as the far-field condition. Then, by integrating Eq. (19) we get the local slip velocity, which is in turn imposed as a boundary condition in solving the system of equations (1d) and (1e). The body-force term $q^*\mathbf{E}^*$ in Eq. (1d) can be evaluated from B2D solutions for $\mathbf{E}^*$ and from Eq. (1c) for q^*.

IV. APPLICATION TO A PAIR OF CIRCULAR CYLINDERS

A. Problem description and analytical and numerical methods for solutions

We consider, as an example of applications, EHD flow around a pair of circular electrodes with radius R submerged in a cavity of height H and length L; see Fig. 3 for the geometric configuration of the problem considered. The RHS electrode is applied with a dc voltage V_a, while the LHS is grounded. It was found that this geometry allows an analytic treatment for the bulk solutions whereas the 1D numerical simulation must be employed for the DSL solutions. We also show in this section how the two solutions match each other at the edge of the DSL.

First, we present the analytical treatment of the bulk equations asymptotically valid for small ε and γ under the
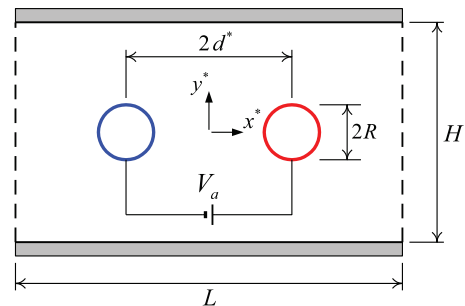

FIG. 3. (Color online) A pair of circular electrodes of radius R submerged in a viscous fluid and subjected to an applied dc voltage, V_a.

assumption of very large cavity; $H/R \gg 1$ and $L/R \gg 1$. For this, we introduce bipolar coordinates $w = \xi + i\eta$ related to the Cartesian coordinates $z = x + iy$ as $w = \ln[(z + c)/(z - c)]$, where $c = \sqrt{d^2 - 1} = \sinh \xi_w$, and $\pm \xi_w = \pm \cosh^{-1} d$ is the value of ξ on the right and left cylinders, respectively. Then the scale factor is given by $|dz/dw| = c/(\cosh \xi - \cos \eta)$. The leading-order equation to be solved for the field is $\nabla \cdot \mathbf{E}_{00} = 0$, or

$$\nabla^2 \phi_{00} = 0, \tag{22}$$

with boundary conditions, $\phi_{00} = 0$ at $\xi = -\xi_w$ (LHS electrode, cathode) and $\phi_{00} = 1$ at $\xi = \xi_w$ (RHS electrode, anode), where the potential ϕ_{00} is related to the field as $\mathbf{E}_{00} = -\nabla \phi_{00}$. The solution is simply $\phi_{00} = (1 + \xi/\xi_w)/2$. Thus, we have

$$\mathbf{E}_{00} = \frac{\cosh \xi - \cos \eta}{-2c\xi_w} \mathbf{e}_\xi, \tag{23}$$

where $\mathbf{e}_\xi$ denotes a unit vector. The next equation to be solved for the potential ϕ_{01} is

$$\nabla^2 \phi_{01} = \mathbf{E}_{00} \cdot \nabla E_{00}. \tag{24}$$

with homogeneous boundary conditions, $\phi_{01} = 0$ at $\xi = \pm \xi_w$. We substitute $\mathbf{E}_{00}$ of Eq. (23) into this and derive the solution as $\phi_{01} = [-\sinh \xi + (\sinh \xi_w/\xi_w)\xi]/(4c\xi_w^2)$ and

$$\mathbf{E}_{01} = \frac{(\cosh \xi - \cos \eta)(\cosh \xi - \sinh \xi_w/\xi_w)}{4c^2 \xi_w^2} \mathbf{e}_\xi. \tag{25}$$

We can also derive the higher-order solution as follows.

$$\mathbf{E}_{02} = E_{02\xi} \mathbf{e}_\xi + E_{02\eta} \mathbf{e}_\eta, \tag{26}$$

$$E_{02\xi} = \frac{(\cosh \xi - \cos \eta)}{96 c^3 \xi_w^3}$$
$$\times \left[-11 \cosh 2\xi + 10(\cosh \xi + \xi \sinh \xi) \cos \eta \right.$$
$$+ \frac{24 \sinh \xi_w}{\xi_w} \cosh \xi - \frac{10 \xi_w \cosh \xi_w}{\sinh \xi_w} \cosh \xi \cos \eta$$
$$\left. + \frac{\sinh \xi_w}{\xi_w^2}(11 \xi_w \cosh \xi_w - 24 \sinh \xi_w) \right], \tag{27a}$$

$$E_{02\eta} = \frac{5(\cosh \xi - \cos \eta) \sin \eta}{48 c^3 \xi_w^3}$$
$$\times \left[-\xi \cosh \xi + \frac{\xi_w \cosh \xi_w}{\sinh \xi_w} \sinh \xi \right]. \tag{27b}$$

Then we obtain the following formula for the space charge density in the bulk.

$$q = \varepsilon \gamma [q_{11} + \gamma q_{12} + O(\gamma^2)] + O(\varepsilon^2), \tag{28}$$

$$q_{11} = \frac{(\cosh \xi - \cos \eta)^2 \sinh \xi}{4 c^3 \xi_w^2}, \tag{29a}$$

$$q_{12} = \frac{(\cosh \xi - \cos \eta)^2 \sinh \xi}{24 c^4 \xi_w^3}$$
$$\times \left(-11 \cosh \xi + 5 \cos \eta + \frac{6 \sinh \xi_w}{\xi_w} \right). \tag{29b}$$

We can see from (23) and (28) that, to the leading order of ε and γ, the Coulomb force $q\mathbf{E}$ is heading from each electrode to the

centerline $x = 0$. As a supplement, it can be shown that the source term, $\nabla q \times \mathbf{E}$, in the equation for the dimensionless vorticity, $\nabla \times \mathbf{u}$, is negative (positive) in the first and third (second and fourth) quadrants, so that the vortical flow should be clockwise (counterclockwise) there; see [33] for detailed derivation of the vorticity equation. We thus expect that the fluid near the centerline would go up in the upper domain $y > 0$ and come down in the lower domain $y < 0$.

The 1D nonlinear DSL equations for the ion transport and potential are then solved by using a separately developed code based on the finite difference method described briefly in Sec. III B; the formulation and numerical-solution methods are general purpose and problem independent, but the quantity E_{0b} at a local point s on the electrode wall to be supplied from the bulk solutions of course depends on the specific geometry concerned. Once the ion concentrations and the potential are derived, the slip velocity is calculated from the numerical integration of Eq. (19).

On the other hand, we also use the commercial software COMSOL to obtain the numerical solutions of the full 2D equations, (1a)–(1e), without approximation (to be called F2D solutions). Three kinds of COMSOL models employed in the simulations are species-transport model for Eqs. (1a) and (1b), electrostatics model for Eq. (1c), and fluid-flow model for Eqs. (1d) and (1e). In order to avoid the numerical instability we use the perturbed variables $\Delta c_\pm^*$ instead of $c_\pm^*$ defined as $c_\pm^* = c_0 \sqrt{F} + \Delta c_\pm^*$ (refer to [23] for details). To resolve the thin DSLs near the electrodes, we employ very fine grids in the proximity of the electrodes. Preliminary test runs were thus needed to attain a proper grid resolution.

B. Results

The liquid used is dodecane mixed with the surfactant Span80 in three proportions: 0.5%, 0.3%, and 0.2%. The liquid mixture shows almost a constant viscosity, $\eta = 1.34$ mPa s. We further set $T = 295$ K, $\varepsilon_p = 2 \times 8.85 \times 10^{-12}$ F m^{-1}, $\bar{a} = 2.25$ nm (averaged ionic radius), and $\kappa_O = m_\pm = 1$. The mobility and the diffusivity are calculated from the formulas $\bar{\mu} = \mu_\pm = e/(6\pi \eta \bar{a})$ and $D_\pm = \zeta_T \mu_\pm$, respectively. We set the geometric parameters as follows: $R = 0.15$ mm, $H = 2.4$ mm, and $L = 12$ mm. Half of the gap spacing between electrodes is set at $d^* = 0.38$ mm for the 0.5% mixture and 0.355 mm for the 0.3% and 0.2% mixtures.

In order to determine the zero-field concentration, we performed a current-voltage experiment for each liquid mixture by using an apparatus with a set of parallel electrodes similar to [12]. The curves of current density versus electric field indeed show enhancement of conductivity at high field following the Onsager effect. Our purpose is to obtain a critical point in the $(c_{\mu 0}, \gamma^*)$ space showing the best curve fitting by using the least-squares method, where $c_{\mu 0} \equiv \bar{\mu} c_0$ is a parameter proportional to the conductivity; in this fitting, we allowed not only the concentration but also the Onsager constant γ^* to be varied. We have found that the rms error associated with the curve fitting is minimized at a critical point as expected, but the value of γ^* at that point is usually less than γ_O^*. More importantly, the low-level contours of rms error show very slender ellipses as shown in Fig. 4 typically for the 0.3% mixture; the other two concentrations
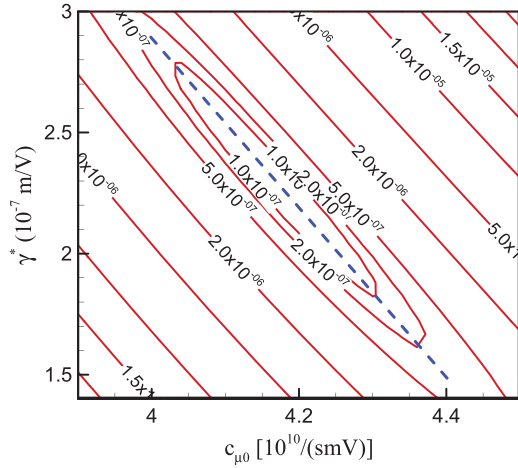
FIG. 4. (Color online) Contours of the rms error, in the $(c_{\mu 0}, \gamma^*)$ space, given in fitting the experimental data of the current-density and electric-field relationship for the 0.3% mixture of dodecane-Span80 by the Onsager function. Note that low levels of rms error are distributed along a straight line, $c_{\mu 0} = (p_1 - 10^7 \gamma^* p_2) \times 10^{10}$ s^{-1} m^{-1} V^{-1} with $p_1 = 4.826$ and $p_2 = 0.2858$ (dashed blue line).

also show similar patterns as this. We derive the principal axis as $c_{\mu 0} = (p_1 - 10^7 \gamma^* p_2) \times 10^{10}$, where $c_{\mu 0}$ and γ^* should be in the units s^{-1} m^{-1} V^{-1} and m V^{-1}, respectively. The two constants used in this equation depend on the liquid mixture and we found $p_1 = 11.35$ and $p_2 = 0.750$ for the 0.5% mixture, $p_1 = 4.826$ and $p_2 = 0.2858$ for the 0.3% mixture, and $p_1 = 3.345$ and $p_2 = 0.188$ for the 0.2% mixture. Instead of choosing γ^* at the critical point for use in the simulation, we may allow it to be varied depending on the problems in hand, e.g., for a better agreement between the simulation and experimental results. Figure 5 illustrates the result of curve fitting with the Onsager function to the experimental data with the critical value $\gamma^* = 2.25 \times 10^{-7}$ m V^{-1}. It is seen that the experimental data are remarkably well reproduced by the
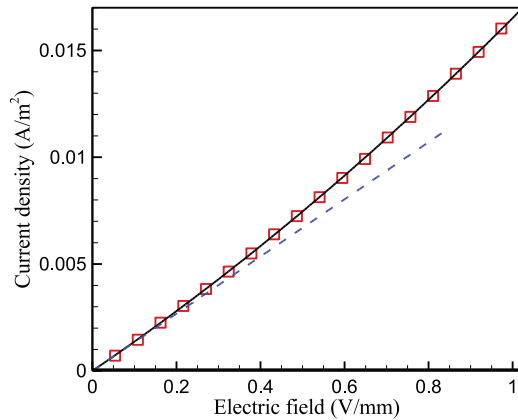

FIG. 5. (Color online) Typical result of the curve fitting by the Onsager function (solid line) with the experimental data (red symbols) for the current-density and electric-field relationship for the 0.3% mixture of dodecane-Span80. The Onsager constant is set at $\gamma^* = 2.25 \times 10^{-7}$ m V^{-1} for this plot. The dashed blue line shows Ohm's law in terms of the zero-field concentration given with the formula presented in the text for the 0.3% mixture.
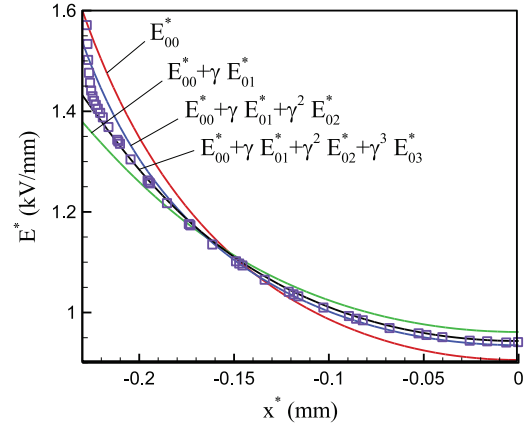

FIG. 6. (Color online) Comparison between the electric-field-intensity distributions along a part of the symmetric line, $y^* = 0$, computed from the asymptotic solutions (solid lines) and that given from the F2D solutions (symbols) for the 0.5% mixture at $V_a = 500$ V and $\kappa_L = 1$.

Onsager function. In this study, however, we do not consider adjustment of γ^* but use the original Onsager constant γ_O^*, that is, κ_O is fixed at 1.

The asymptotic bulk solutions given in Sec. IV A may be useful as benchmark solutions (for example, in validating numerical simulation results). Figure 6 shows a comparison between the electric-field distribution along a line segment on $y^* = 0$ obtained from F2D and from the asymptotic solutions (23), (25), and (26); the solution $\mathbf{E}_{03}$ was also obtained but is not presented in this paper. We can see that the asymptotic solution tends toward the numerical solution as the number of terms is increased in the analysis. With the parameter set used for this result, we can evaluate the perturbation parameter as $\varepsilon = 7.2 \times 10^{-4}$ being much smaller than 1, which ensures that the leading-order solutions for ε are accurate enough. On the other hand, we get $\gamma = 0.96$ (or as a more reasonable quantity, $\gamma E = 0.43$ based on the maximum value of E^* taken from Fig. 6), a result which is seemingly contradictory to the requirement, $\gamma \ll 1$, for the validity of the perturbation methods with the expansion of variables in terms of γ. Nevertheless, it is found to provide accurate solutions with four leading terms as shown in Fig. 6, confirmatively because the expansion of the Onsager function (2) has infinite radius of convergence.

Validity of the 1D model for the DSL is next confirmed from a comparison of the 1D simulation results and those given from F2D as shown in Figs. 7(a) and 7(b) obtained at $\kappa_L = 1$, and Figs. 7(c) and 7(d) obtained at $\kappa_L = 0.1$; in the 1D simulation, the value of E_{0b} at the edge of the DSL is supplied from the 2D bulk solutions, B2D. They are again remarkably in good agreement with each other. Such excellent agreement is of course indebted to the fact that ε remains small enough.

At a lower κ_L [Figs. 7(c) and 7(d)], the counterion (i.e., cation) concentration within the DSL is less than the bulk value. In order to help understand such peculiar results, we have derived the asymptotic solutions valid for large Y (see Appendix B). The solutions (A3a) and (A3b), indicate that as κ_L decreases f_w is decreased whereas $-h_w$ is increased, being consistent with Fig. 2. Further, the critical value of κ_L at which
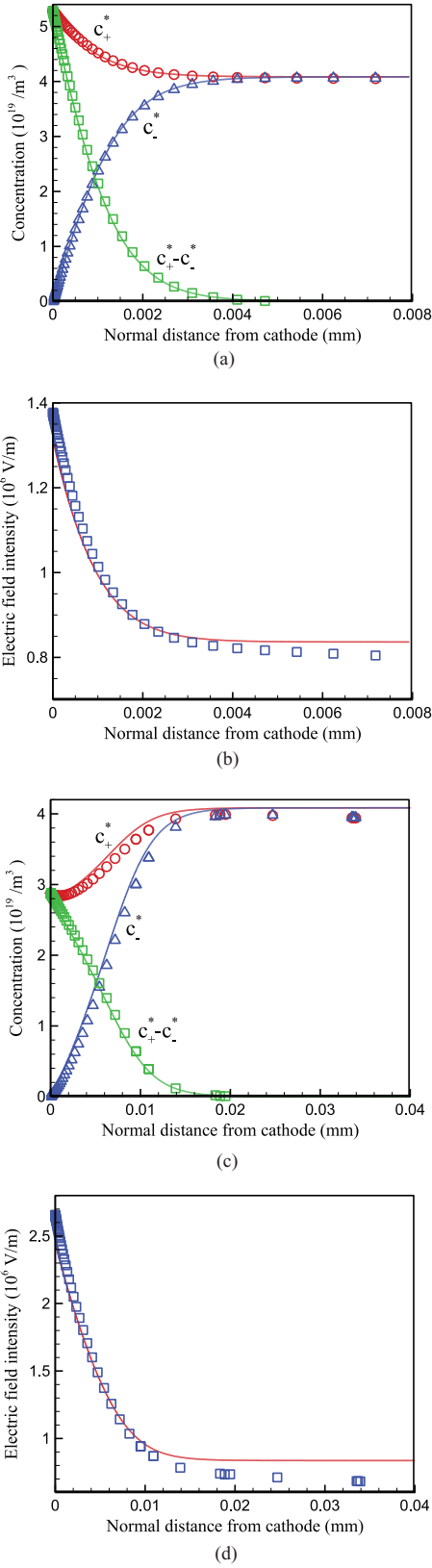
(a)

(b)

(c)

(d)

FIG. 7. (Color online) Distribution of concentrations (a), (c) and electric-field intensity (b), (d) along the normal distance to the cathode measured from the point $(x,y) = (-d,1)$. Solid lines are computed from the 1D simulation of the DSL equations, (16a)–(16c), and the symbols from F2D for the 0.5% mixture at $V_a = 500$ V and $\kappa_L = 1$ in (a) and (b) and $\kappa_L = 0.1$ in (c) and (d).
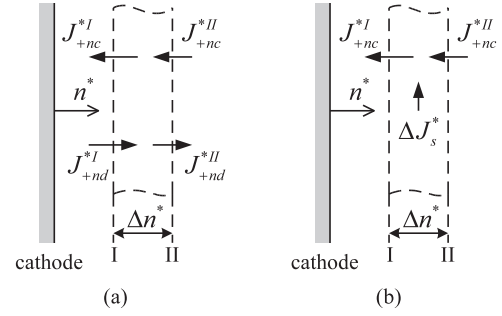

(a)   (b)

FIG. 8. Counterion fluxes through two sections, I and II, separated by a small distance Δn^* and located close and parallel to the cathode, (a) within the diffuse layer of the EDL with polar fluid and (b) within the DSL with nonpolar fluid.

perturbation to f_w vanishes is predicted to be $\kappa_L = 0.5$, which was also confirmed by Fig. 2 and the related discussion given in Sec. III B.

Lowering of the counterion concentration in the thin layer near the electrode below the value at the edge of the layer is not possible for the ion transport within the diffuse layer of EDL with polar fluid. Within the diffuse layer of the EDL, the total normal flux of the counterion concentration through a sectional plane normal to the electrode wall, which is given by the sum of the conductive normal flux, $J_{+nc}^* = \mu_+ E_n^* c_+^*$, and the diffusive normal flux, $J_{+nd}^* = -D_+ \partial c_+^*/\partial n^*$, must be zero; $J_{+nc}^* + J_{+nd}^* = 0$. Since E_n^* is negative when the coordinate n^* has its origin at the cathode (Fig. 8) and c_+^* is positive, it is expected that $J_{+nc}^* < 0$ and $J_{+nd}^* > 0$ leading to $\partial c_+^*/\partial n^* < 0$. This means that the cation concentration must decrease monotonically with n^* near the cathode. Figure 8(a) illustrates the variation of the ionic fluxes through an imaginary slab of small thickness Δn^*. On the other hand, within the DSL of nonpolar fluid, the spatial gradient of the conductive flux is balanced by the ion source; $\partial J_{+nc}^*/\partial n^* \cong \Delta J_s^*/\Delta n^*$, where $\Delta J_s^* = \kappa_L \alpha_L (c_0^{*2} - c_+^* c_-^*) \Delta n^*$ [Fig. 8(b)]. Since $\Delta J_s^* > 0$, we arrive at $\partial J_{+nc}^*/\partial n^* > 0$ indicating that $-J_{+nc}^*$ should
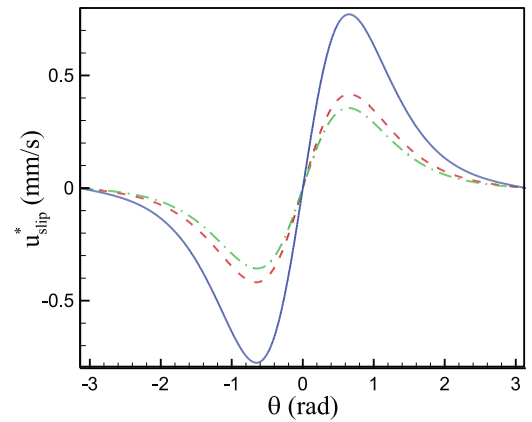

FIG. 9. (Color online) Contribution of the osmotic-pressure-driven slip velocity (dashed red line) and that of the tangential Coulomb-force component (dash-dot green line) to the total slip velocity (solid blue line) around the LHS cylinder calculated from double integration of Eq. (19) with the field distribution E_{0b} obtained from B2D for the 0.5% mixture at $V_a = 500$ V and $\kappa_L = 0.5$.
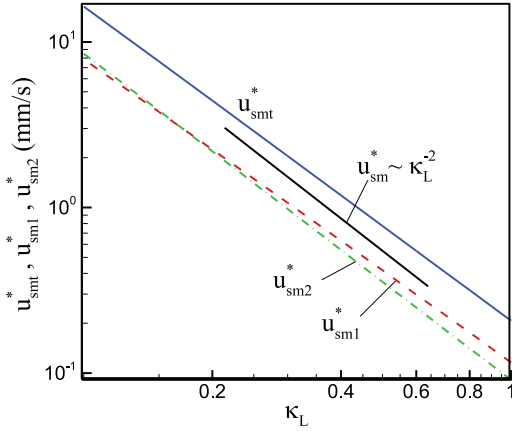
FIG. 10. (Color online) Variation of $u^*_{smt}(= u^*_{sm1} + u^*_{sm2})$, maximum value of u^*_{slip} over the half circle $0 \leqslant \theta \leqslant \pi$, upon the change of κ_L. The other parameters are set the same as in Fig. 9. Also shown are u^*_{sm1}, the osmotic-pressure-driven slip velocity (dashed red line), and u^*_{sm2}, the tangential-Coulomb-force-driven slip velocity (dash-dot green line).

decrease with n^* as illustrated in Fig. 8(b). As κ_L is decreased, ΔJ^*_s decreases accordingly and the gradient $\partial J^*_{+nc}/\partial n^*$ also decreases. In view of $J^*_{+nc} = \mu_+ E^*_n c^*_+$ we can see that when $-E^*_n$ decreases so rapidly with n^* it can happen that c^*_+ should rather increase with n^*, as in the case shown in Fig. 7(b).

We have shown that the dimensionless slip velocity u_{slip} can be obtained from double integration of Eq. (19) with respect to n. For the 0.5% solution, B2D was run to get E_{0b} around each electrode, which was then substituted into Eq. (19) and integrated twice over $0 \leqslant n \leqslant n_\infty$, where n_∞ was taken large enough so that $\hat{h}^2 - 1$ and $\hat{f} - \hat{g}$ asymptotically vanish there with enough accuracy. Figure 9 shows a typical distribution of u^*_{slip} on the LHS cylinder. We see that $u^*_{slip} > 0$ over $0 < \theta < \pi$ [θ is angle measured from the facing stagnation point of the LHS cylinder at $(x,y) = (1 - d, 0)$] and $u^*_{slip} < 0$

over $-\pi < \theta < 0$. This means that the slip velocity on the cylindrical electrodes causes the fluid adjacent to the electrodes to move away from the facing stagnation point, which tends to drive the fluid near the vertical line $x = 0$ toward the origin of the coordinates contrary to the role of the bulk-charge density. We will see that the slip velocity is the root of the DSL vortex. Figure 9 also reveals that the contribution of the osmotic pressure to the total slip velocity is almost at the same level as that of the tangential Coulomb-force component.

In order to explore the effect of the reduction of the Langevin constant on the slip velocity, we plotted the variation of the maximum slip velocity on the LHS electrode as a function of κ_L as shown in Fig. 10. Thus, the slip velocity scales almost at $u^*_{slip} \sim \kappa_L^{-2}$ over such wide range of κ_L being consistent with Eq. (20). It also shows again that contribution of the osmotic pressure to the slip velocity is almost at the same level as that of the tangential component of the Coulomb force over the whole range of κ_L.

We now present a qualitative and quantitative comparison between the numerical and experimental results. The experimental streamlines of Fig. 11(a) obtained for the 0.5% solution indicate that the flow field is dominated by the bulk-driven flow, and fluid near the vertical centerline $x^* = 0$ goes up in the upper region $y^* > 0$ and comes down in the lower region $y^* < 0$ as predicted in Sec. IV A. The F2D result [Fig. 11(b)] given at $\kappa_L = 0.3$ well reproduces the experimental one. In this solution mixture, the numerical simulation with a different κ_L gives the pattern indistinguishable from Fig. 11(b) and the quantitative difference is also insignificant; for instance, the vertical velocity component at $(x^*, y^*) = (0, 0.6)$ mm becomes $v^*_c = 4.5$ mm s^{-1} at $\kappa_L = 0.3$ and $v^*_c = 5.0$ mm s^{-1} at $\kappa_L = 1$ showing only a 10% difference. Figure 12 reveals the 1D distribution of the vertical velocity component, denoted as v^*_{1D}, along the horizontal line $y^* = 0.6$ mm, obtained by particle tracking velocimetry (PTV) measurement and F2D with the same parameter set as in Fig. 11(b). Considering that in most studies on electrokinetics quantitative comparison between the numerical and experimental results was not as

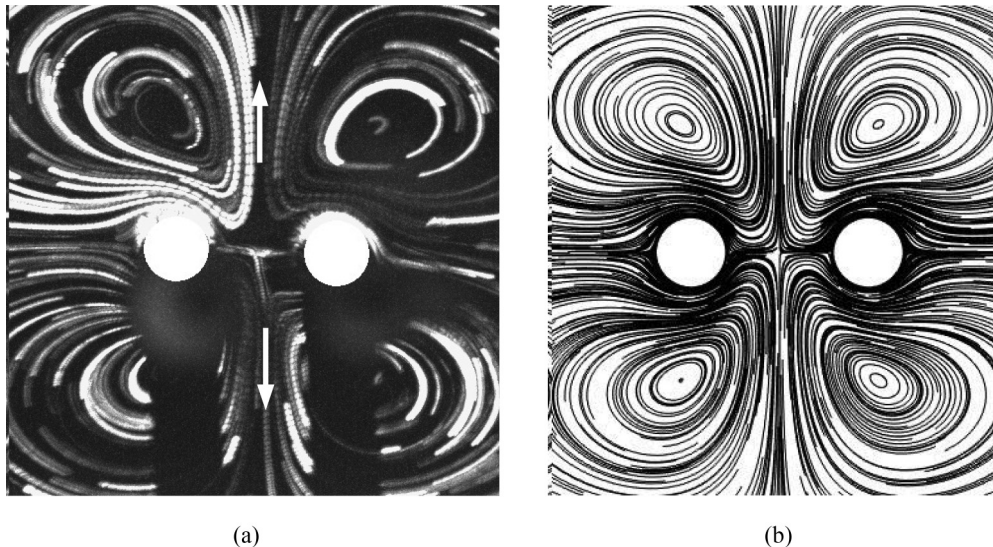(a)   (b)

FIG. 11. Streamlines obtained from (a) flow-visualization experiment and (b) numerical simulation for the 0.5% mixture at 500 V. Numerical result is obtained at $\kappa_L = 0.3$.
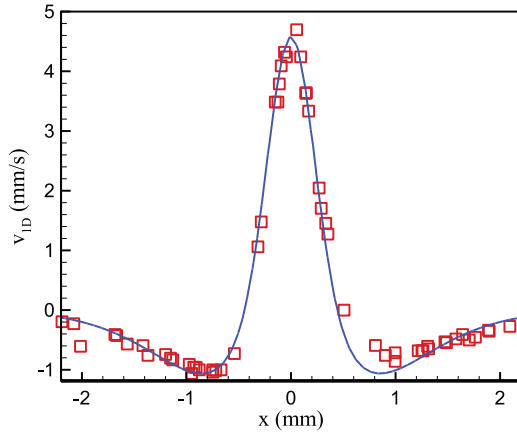
FIG. 12. (Color online) 1D distribution of the vertical velocity component at $y^* = 0.6$ mm obtained from PTV experiment (red symbols) and numerical simulation (solid blue line) with the same parameter set as in Fig. 11.

consistent [30–35], we can say that the agreement between the two results shown in Fig. 12 is quite excellent.

Equations (20) and (13) indicate that as the concentration of the surfactant Span80 in the mixture is decreased (that is, as c_0 is decreased), the DSL effect is increased through the increase of the DSL-driven slip velocity, whereas the bulk-driven flow is unaffected. Figure 13 shows the streamline patterns obtained for 0.3% and 0.2% mixtures at 400 V. Compared with the case of the 0.5% mixture (Fig. 11), the DSL-driven slip velocity for the 0.3% mixture is large enough to cause the emergence of two new vortices (to be referred to as DSL vortices) around the electrodes [Figs. 13(a) and 13(b)]; the streamline patterns at $V_a = 500$ V are qualitatively the same as the patterns of Fig. 13 given at 400 V for both mixtures. Although the DSL vortices are almost of the same size as the electrodes, the thickness of DSL is only 10% of the cylinder radius. This ensures that the DSL vortex is indeed an outcome of the slip velocity at the edge of the DSL. In the case of the 0.2% mixture, Figs. 13(c) and 13(d), the whole domain is now dominated by the DSL vortices and we observe a flow reversal; the fluid near the vertical centerline comes down in the upper region $y^* > 0$ and goes up in the lower region, contrary to the case with the 0.5% mixture (Fig. 11). Notice that the DSL still remains thin, about 0.02 mm, and thus the resultant flow should be categorized
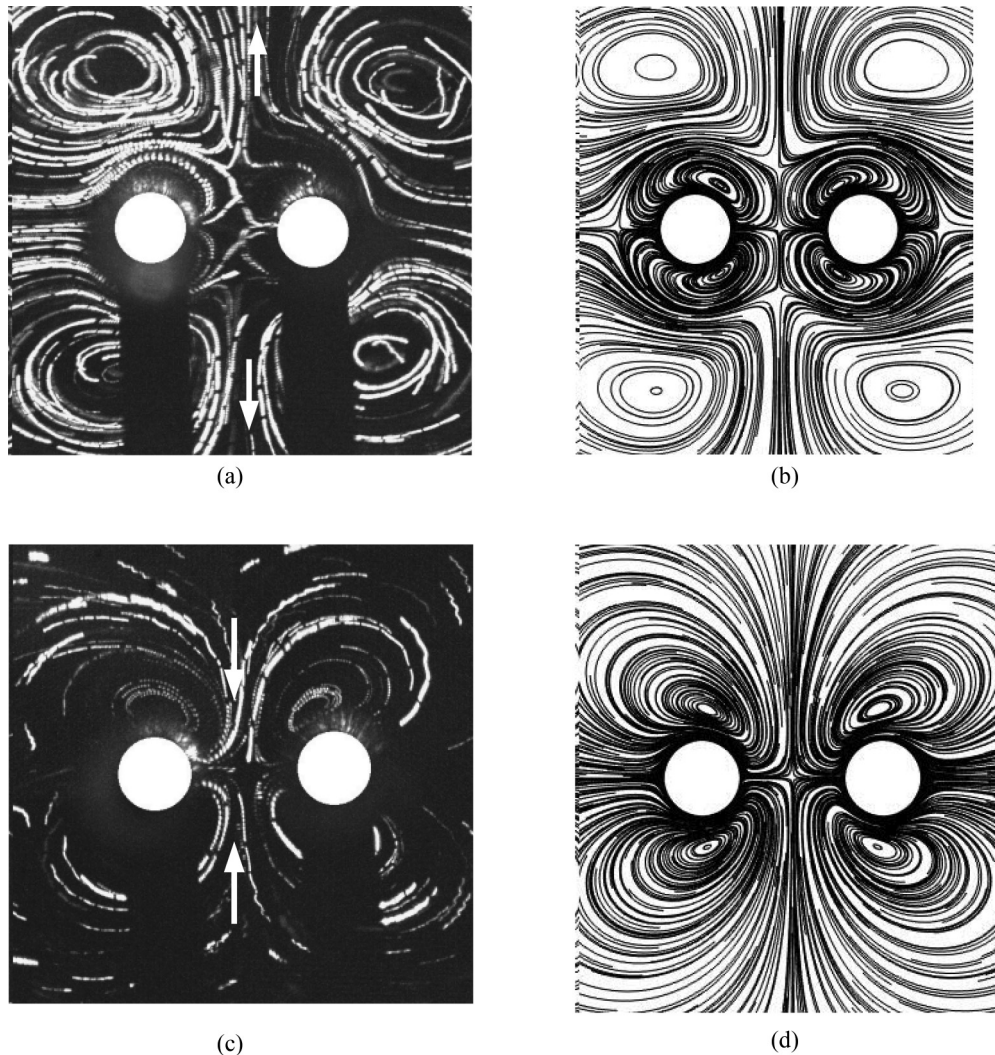

(a)

(b)

(c)

(d)

FIG. 13. Experimental (a), (c) and numerical (b), (d) streamlines for the 0.3% (a), (b) and 0.2% (c), (d) mixtures at 400 V. Numerical results are obtained at $\kappa_L = 0.174$ in (b) and $\kappa_L = 0.168$ in (d).
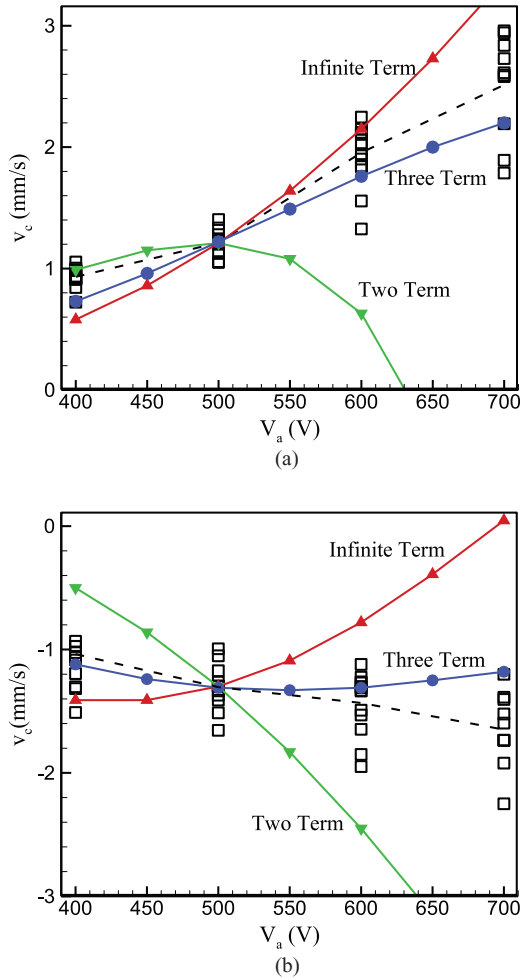
FIG. 14. (Color online) Experimental (scattered square symbols) and numerical (solid lines with symbols) results of v_c^* for (a) 0.3% and (b) 0.2% mixtures; v_c^* is the vertical velocity component at the point $(x^*, y^*) = (0, 0.7)$ mm in (a) and $(0, 0.25)$ mm in (b). Dashed lines denote the experimental data averaged at each V_a. In the numerical simulation, three different numbers of leading terms are used in the series representation of the Onsager function [Eq. (2) in the text]. $\kappa_L = 0.331, 0.203$, and 0.174 are used in (a) and $\kappa_L = 0.354, 0.205$, and 0.168 in (b) for the two-, three-, and infinite-term expansion, respectively; these are determined so as to match the experimental data at $V_a = 500$ V with each expansion.

as induced-charge electro-osmosis (ICEO) [30–36]; further discussion on the different features between the conventional ICEO with polar liquid and that with nonpolar liquid will be given in the last part of this section. For both mixtures, the numerical streamlines again appear to be in good agreement with the experimental ones.

As predicted previously, a decrease of the factor κ_L brings an increase of the DSL-driven slip velocity. We also revealed, in the case of the 0.5% solution (Fig. 11), that the velocity measured from the experiment can be matched with the numerical solution by adjusting the parameter κ_L in the simulation. However, it turns out that κ_L, while providing a successful matching at one voltage, does not result in a satisfactory matching at another voltage. Figure 14 demonstrates this for the 0.3% and 0.2% mixtures. For the 0.3% mixture [Fig. 14(a)],

F2D with $\kappa_L = 0.174$ yields $v_c^* = 1.21$ mm/s that exactly matches the experimental result at $V_a = 500$ V, where v_c^* is now the vertical velocity component at $(x^*, y^*) = (0, 0.7)$ mm. However F2D with the same κ_L overestimates the experimental data at larger voltages and underestimates at smaller voltages when the original Onsager function is used. A similar trend is observed in the 0.2% mixture as shown in Fig. 14(b); in this case, the numerical simulation gives $v_c^* = -1.30$ mm s^{-1} at $(x^*, y^*) = (0, 0.25)$ mm with $\kappa_L = 0.168$ for $V_a = 500$ V, which exactly matches the experimental data. These results imply that truncation of the series for the Onsager function after a few terms may improve the matching, because the resultant function should be always lower than the original Onsager function. Figures 14(a) and 14(b) show that the numerically given v_c^* with three-term expansion for the Onsager function indeed matches the experimental data better than with the original (infinite-term) function for the range of voltage, 400−700 V; here the two-term expansion corresponds to overtruncation. Since the Onsager function is responsible for the charge generation, we may argue from the above reasoning that the Onsager function in its original form, Eq. (2), tends to overestimate the charge generation.

As described at the end of Sec. III, we can apply the slip-velocity model in 2D simulation of EHD flows by combining the bulk and DSL solutions. Figure 15 shows a comparison between v_c^* obtained from the F2D simulation and that from the slip-velocity model. We can see that the slip-velocity model slightly overpredicts the F2D results but otherwise the former closely follows the trend of the latter. On the other hand, the conventional B2D without the DSL effect (horizontal straight line in Fig. 15) cannot successfully reproduce the F2D data, in particular at small κ_L, for which the DSL effect is estimated to be considerable. The same argument holds for the cases with low concentration or small-scale geometry, where the DSL effect becomes relatively large or u_{slip}^*/u_b^* is large, as can be seen from Eq. (21). That is, the B2D solutions alone, as used in [10,20], cannot predict DSL vortices or flow reversal of Fig. 13.
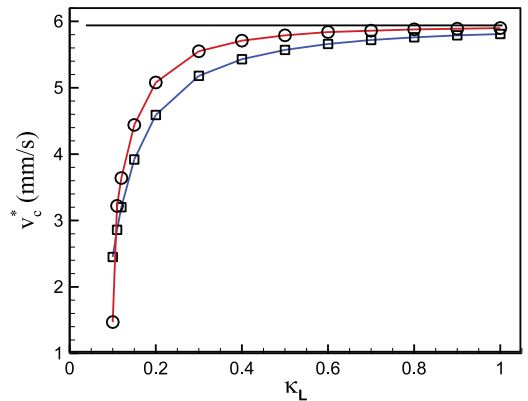

FIG. 15. (Color online) Comparison between the simulation result with the slip-velocity model (red solid line with circles) and that with the full F2D (blue solid line with squares) in terms of v_c^*, the vertical velocity at $(x^*, y^*) = (0, 0.5)$ mm, obtained for the 0.5% mixture at 500 V with various κ_L. The solid straight line corresponds to the simulation result, $v_c^* = 5.94$ mm s^{-1}, obtained from the conventional bulk-solution method without considering the DSL effect, i.e., B2D.
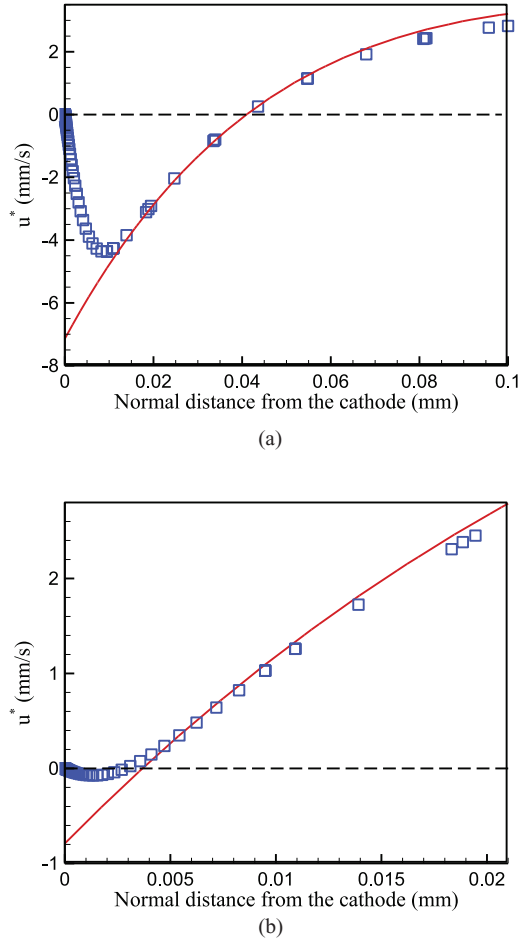
(a)

(b)

FIG. 16. (Color online) Distribution of the tangential velocity component u^*, along the normal distance from the point $(x^*, y^*) = (-d^*, R)$ on the cathode wall, for the 0.5% mixture at 500 V with (a) $\kappa_L = 0.1$ and (b) $\kappa_L = 0.3$. Blue symbols correspond to the F2D data and the solid red lines to the slip-velocity-model solutions. Note $d^* = 0.38$ mm for the 0.5% mixture.

The advantage of the slip-velocity model compared with the full model is obvious; firstly, we do not need to solve the ion-transport equations for the bulk region, and secondly, since the DSL is well resolved by using a separate program for the 1D equations, the numerical simulation for the bulk, B2D, is still free from constructing extremely fine grids near the electrodes.

In order to capture the extent of the DSL within the DSL vortex and to understand the way the DSL solutions match the bulk solutions, we plot the 1D distribution of the tangential velocity component along the normal distance from a point on the LHS electrode as shown in Fig. 16. We can confirm the asymptotic approach of the velocity from the sharp increase near the wall to the slow variation in the bulk in particular with $\kappa_L = 0.1$ [Fig. 16(a)]. From Fig. 16(a), we measure the thickness of the DSL as about 0.015 mm, and this is considerably smaller than the size of the DSL vortex, 0.1 mm, which means that the DSL is completely embedded in the DSL vortex. On the other hand, for $\kappa_L = 0.3$ [Fig. 16(b)] the slip velocity is much smaller than Fig. 16(a) and thus the DSL thickness is comparable to the size of the DSL vortex. In summary, the DSL vortex can be said to be a manifestation of the induced-charge electro-osmotic

TABLE I. Comparison of important features of induced-charge electro-osmotic flow (ICEO) between polar and nonpolar fluids. The formula showing the velocity's dependence on the field, scale, and concentration applies only when the corresponding layers (indicated by ∗) are thin enough compared with the bulk.

Fluid		Polar [30–36]	Nonpolar [10,20,22,23]	
Electrical permittivity		High	Low	
Electric field		Low	High	
Effective with ac or dc?		ac (dc)	ac (dc)	
Relevant scale		nm to μm	μm to mm	
Charge-induced region		Double layer∗	Bulk	DSL∗
Velocity's	Field	$\sim E^2$	$\sim E^3$	$\sim E^4$
dependence on	Scale	$\sim R$	$\sim R$	$\sim R^{-1}$
	Concentration	–	–	$\sim c_0^{-2}$

flow driven by the thin DSL, and its size is dependent on the competition between the bulk-charge-induced flow and the DSL-charge-induced slip velocity.

Now we can compare the key elements of the conventional ICEO for polar fluid (PF-ICEO) and those of the present study for the nonpolar fluid (NF-ICEO) as shown in Table I. Since the body force in the Stokes equations takes the same form in both flow types, i.e., product of charge density and field, either ac or dc can be applied to yield ICEO; however, dc is not practical in PF-ICEO because of the degradation of electrodes. In PF-ICEO, the Onsager effect is not concerned because the applied field is in a low level, and so the flow is induced only within the double layer. Most distinctively, the double layer in PF-ICEO is an outcome of the balance between the diffusion and conduction (ion migration) terms in the ion-transport equations [30–36], whereas the DSL in NF-ICEO is that between the conduction and ion-dissociation terms. Similar to PF-ICEO, the bulk-driven velocity is proportional to the scale in NF-ICEO. On the contrary, the DSL-driven velocity is proportional to the inverse of the scale, so it should dominate over the bulk-driven flow as the scale is decreased. Dependence of the flow velocity on the field is the weakest in the PF-ICEO ($\sim E^2$) and the most pronounced in the DSL-driven ICEO ($\sim E^4$). Compared with the other two velocities, the DSL-driven slip velocity in the NF-ICEO is expected to increase with a decrease in concentration.

V. CONCLUSIONS

We performed an asymptotic analysis for the charge-transport and fluid-flow problems of dielectric liquid under the limit of small ε and small γ. We have derived a series of governing equations valid to $O(\varepsilon)$ in linear form that are used to hierarchically obtain the electric field and ion concentrations in the bulk. The analysis justifies the use of simplified but nonlinear equations (B2D) for the bulk electric field encompassing the Onsager effect, which is valid only if the DSL effect is negligible. The order-of-magnitude analysis shows that the bulk-charge-induced flow velocity is proportional to the geometric scale and cubic power of the applied field independent of the ion concentration, in line with [10,20].

We have also derived 1D nonlinear equations for the ion-transport problem within DSL that should be practically solved with a numerical method. It was found that the DSL thickness is proportional to the applied electric field and inversely proportional to the zero-field ion concentration. Thus, we expect that, without additives such as Span80, the ion concentration tends to vanish and the EHD flow should be dominated by DSL-charge-driven electro-osmotic flow.

We have further derived a formula to be integrated twice on the normal coordinate to obtain the slip velocity at the edge of the DSL. The slip velocity turns out to be proportional to the fourth power of the field and inversely proportional to the geometric scale and the quadratic power of concentration. One of the most important consequences of the asymptotic analysis is given as Eq. (21). Dominance of the DSL-driven flow over the bulk-driven flow is increased as the electric field is increased and the geometric scale or the ion concentration is decreased. It also reveals that decrease of the Onsager's dissociation effect and the recombination rate also causes the DSL-driven flow to be more dominant.

Application of the analysis to the EHD flow over a pair of circular electrodes presents closed-form solutions for the bulk electric field and charge density. The dimensionless leading-order charge density is found to be $O(\varepsilon\gamma)$. The vortical flow was predicted to be clockwise (counterclockwise) in the first and third (second and forth) quadrants of the domain, which was also confirmed from experimental visualization and numerical simulation. Numerical solutions of the DSL equations are also shown to be in good agreement with the results obtained with F2D, confirming the validity of both solution methods.

Flow solutions obtained from numerical simulation with the full 2D equations compare well with the experimental ones for the 0.5% mixture not only qualitatively but also quantitatively, and the flow structure is consistent with our prediction from the asymptotic analysis. It turns out that the contribution of the osmotic pressure to the slip velocity at the edge of the DSL is at the same level as that of the tangential Coulomb-force component.

The experimentally observed flow reversal at lower mixture concentrations could be well captured by F2D with reduced recombination constants. The conventional EHD flow simulation method with only B2D, in which the DSL effect is neglected, cannot reproduce such flow reversal because the flow reversal is caused by the increase of the DSL-driven slip velocity, which counteracts the bulk-charge-driven flow in particular near the electrodes. The DSL is confined within the DSL vortex with its thickness being much smaller than the size of DSL vortex, implying that the apparent extent of the DSL vortex should not be confused with the DSL region.

In this study, the role of the reduction factor for the recombination constant, κ_L, in the DSL solution was also clarified. As the factor is decreased, the slip velocity increases due to the increase of the DSL thickness and the field intensity in the DSL. Adjustment of κ_L is thus mandatory for matching between the experimental and numerical solutions.

Further, we have also numerically shown that the Onsager function in its original form tends to overestimate the charge generation. This conclusion is drawn from the requirement that the experimentally measured velocities at different applied voltages should be reproduced with the same value of κ_L. Further study is needed to see if the same argument holds for different geometric variations, such as coplanar electrodes.

APPENDIX A: DERIVATION OF H_{ij}

We need to expand $F(E)$ in terms of the expansion parameters ε and γ. For this, we write

$$E = |\mathbf{E}_0 + \varepsilon\mathbf{E}_1 + \varepsilon^2\mathbf{E}_2 + \cdots| = H_0 + \varepsilon H_1 + \varepsilon^2 H_2 + \cdots,$$

where each term in the expansion $H_i = \sum_{j=0}^{\infty} \gamma^j H_{ij}$ is to be written in terms of E_{ij}. Then, we get

$$E^2 = H_0^2 + 2\varepsilon H_0 H_1 + \varepsilon^2(2H_0 H_2 + H_1^2) + \cdots.$$

Equating this with the expansion of $\mathbf{E} \cdot \mathbf{E}$ where we use the double expansion for $\mathbf{E}$, we get

$$H_{00} = E_{00}, \quad H_{01} = \frac{\mathbf{E}_{00} \cdot \mathbf{E}_{01}}{E_{00}},$$

$$H_{02} = \frac{2\mathbf{E}_{00} \cdot \mathbf{E}_{02} + E_{01}^2 - H_{01}^2}{2E_{00}}, \quad H_{10} = \frac{\mathbf{E}_{00} \cdot \mathbf{E}_{10}}{E_{00}},$$

$$H_{11} = \frac{\mathbf{E}_{00} \cdot \mathbf{E}_{11} + \mathbf{E}_{01} \cdot \mathbf{E}_{10} - H_{01} H_{10}}{E_{00}},$$

$$H_{12} = \frac{\mathbf{E}_{00} \cdot \mathbf{E}_{12} + \mathbf{E}_{01} \cdot \mathbf{E}_{11} + \mathbf{E}_{02} \cdot \mathbf{E}_{10} - H_{01} H_{11} - H_{02} H_{10}}{E_{00}},$$

$$H_{20} = \frac{2\mathbf{E}_{00} \cdot \mathbf{E}_{20} + E_{10}^2 - H_{10}^2}{2E_{00}},$$

$$H_{21} = \frac{\mathbf{E}_{00} \cdot \mathbf{E}_{21} + \mathbf{E}_{01} \cdot \mathbf{E}_{20} + \mathbf{E}_{10} \cdot \mathbf{E}_{11} - H_{01} H_{20} - H_{10} H_{11}}{E_{00}}.$$

APPENDIX B: DERIVATION OF THE ASYMPTOTIC SOLUTIONS OF EQS. (16a)–(16c) FOR LARGE Y

For $m_{\pm} = 1$ and $\gamma \ll 1$, we can write Eqs. (16a)–(16c) as

$$\frac{d}{dY}(\hat{h}\,\hat{f})' = 1 - \hat{f}\,\hat{g}, \tag{B1a}$$

$$-(\hat{h}\,\hat{g})' = 1 - \hat{f}\,\hat{g}, \tag{B1b}$$

$$2\kappa_L \hat{h}' = \hat{f} - \hat{g}, \tag{B1c}$$

where the prime denotes the derivative with respect to Y; $\varphi' = d\varphi/dY$. Next, we consider perturbation of the variables from the bulk values $(\hat{f},\hat{g},\hat{h}) = (1,1,-1)$; $\hat{f} = 1 + \Delta f$, $\hat{g} = 1 + \Delta g$, and $\hat{h} = -1 + \Delta h$. Substituting these into Eqs. (A1a)–(A1c) and neglecting product of small-order terms,

we get

$$\Delta f' - \Delta h' = \Delta f + \Delta g, \quad \Delta g' - \Delta h' = -(\Delta f + \Delta g),$$
$$2\kappa_L \Delta h' = \Delta f - \Delta g.$$

This constitutes a linear system of ordinary differential equations, and we can find the solutions easily;

$$\hat{f} = 1 + \frac{\sqrt{2\kappa_L} - 1}{\sqrt{2\kappa_L} + 1} \exp(-\lambda Y), \tag{B2a}$$

$$\hat{g} = 1 - \exp(-\lambda Y), \tag{B2b}$$

$$\hat{h} = -1 - \frac{1}{\sqrt{2\kappa_L} + 1} \exp(-\lambda Y), \tag{B2c}$$

where $\lambda = \sqrt{2/\kappa_L}$, and the boundary condition $\hat{g} = 0$ at $Y = 0$ is applied to determine the unknown constant. The wall values are then derived as follows.

$$f_w = 1 + \frac{\sqrt{2\kappa_L} - 1}{\sqrt{2\kappa_L} + 1}, \tag{B3a}$$

$$-h_w = 1 + \frac{1}{\sqrt{2\kappa_L} + 1}. \tag{B3b}$$

[1] M. Zdanowski, IEEE Trans. Dielectr. Electr. Insul. **15**, 527 (2008).

[2] J. M. Cabalerio, T. Paillat, O. Moreau, and G. Touchard, IEEE Trans. Ind. Appl. **45**, 597 (2009).

[3] C. Tang, G. Chen, M. Fu, and R. Liao, IEEE Trans. Dielectr. Electr. Insul. **17**, 775 (2010).

[4] B. Comiskey, J. D. Albert, H. Yoshizawa, and J. Jacobson, Nature **394**, 253 (1998).

[5] M. E. Parent, J. Yang, Y. Jeon, M. F. Toney, Z.-L. Zhou, and D. Henze, Langmuir **27**, 11845 (2011).

[6] S. Jeong and J. Seyed-Yagoobi, IEEE Trans. Ind. Appl. **39**, 355 (2003).

[7] Y. Feng and J. Seyed-Yagoobi, Phys. Fluids **16**, 2432 (2004).

[8] M. R. Pearson and J. Seyed-Yagoobi, IEEE Trans. Dielectr. Electr. Insul. **16**, 424 (2009).

[9] R. V. Raghavan, J. Qin, L. Y. Yeo, J. R. Friend, K. Takemura, S. Yokota, and K. Edamura, Sens. Actuators, B **140**, 287 (2009).

[10] W. Kim, J. C. Ryu, Y. K. Suh, and K. H. Kang, Appl. Phys. Lett. **99**, 224102 (2011).

[11] A. Dukhin and P. J. Goetz, J. Electroanal. Chem. **588**, 44 (2006).

[12] J. K. Park, J. C. Ryu, W. K. Kim, and K. H. Kang, J. Phys. Chem. B **113**, 12271 (2009).

[13] A. Castellanos, *Electrohydrodynamics* (Springer-Verlag, New York, Wien, 1998).

[14] Y. K. Suh, IEEE Trans. Dielectr. Electr. Insul. **19**, 831 (2012).

[15] L. Onsager, J. Chem. Phys. **2**, 599 (1934).

[16] A. P. Persoons, J. Phys. Chem. **78**, 1210 (1974).

[17] V. Adamec and J. H. Calderwood, J. Phys. D: Appl. Phys. **10**, L79 (1977).

[18] Z. Randriamalala, A. Denat, J. P. Gosse, and B. Gosse, IEEE Trans. Electr. Insul. **EI-20**, 167 (1985).

[19] F. Pontiga and A. Castellanos, IEEE Trans. Ind. Appl. **32**, 816 (1996).

[20] J. C. Ryu, H. K. Park, and K. H. Kang, Phys. Rev. Lett. **104**, 104502 (2010).

[21] D. A. Saville, Annu. Rev. Fluid Mech. **29**, 27 (1997).

[22] S. I. Jeong and J. Seyed-Yagoobi, IEEE Trans. Electr. Insul. **11**, 899 (2004).

[23] Y. K. Suh and K. H. Baek, Phys. Rev. E **87**, 023009 (2012).

[24] F. E. Bailey and A. Patterson Jr., J. Am. Chem. Soc. **74**, 4756 (1952).

[25] N. Pannacci, E. Lemairea, and L. Lobry, Eur. Phys. J. E **28**, 411 (2009).

[26] G. B. Briere, Br. J. Appl. Phys. **15**, 413 (1964).

[27] A. I. Zhakin, Phys.-Usp. **46**, 45 (2003).

[28] C. W. Wu and H. Conrad, J. Phys. D: Appl. Phys. **31**, 3403 (1998).

[29] R. F. Probstein, *Physicochemical Hydrodynamics: An Introduction* (Wiley-Interscience, Hoboken, NJ, 2003).

[30] T. M. Squire and M. Z. Bazant, J. Fluid Mech. **509**, 217 (2004).

[31] Y. K. Suh and S. Kang, Phys. Rev. E **77**, 031504 (2008).

[32] Y. K. Suh and S. Kang, Phys. Rev. E **79**, 046309 (2009).

[33] Y. K. Suh, Colloid Surf., A **376**, 111 (2011).

[34] A. J. Pascall and T. M. Squires, Phys. Rev. Lett. **104**, 088301 (2010).

[35] M. Z. Bazant and T. M. Squires, Curr. Opin. Colloid Interface Sci. **15**, 203 (2010).

[36] M. M. Gregersen, F. Okkels, M. Z. Bazant, and H. Bruus, New J. Phys. **11**, 075019 (2009).